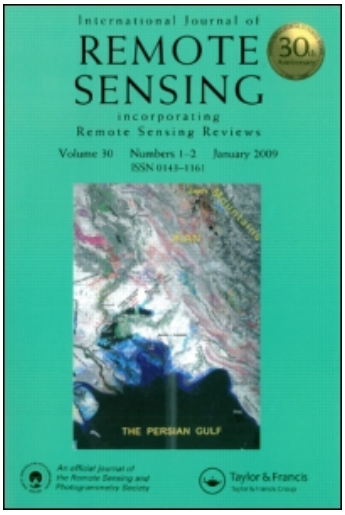

International Journal of Remote Sensing
Publication details, including instructions for authors and subscription information:
http://www.informaworld.com/smpp/title~content=t713722504

Wind and wave observations off the south Pacific Coast of Mexico using TerraSAR-X imagery

Guillermo M. Díaz Méndez[a]; Susanne Lehner[b]; Francisco J. Ocampo-Torres[c]; Xiao Ming Li[b]; Stephan Brusch[b]
[a] Faculty of Marine Sciences, Universidad Autonoma de Baja California (UABC), Ensenada, Mexico [b] Remote Sensing Technology Institute, Deutsches Zentrum für Luft-und Raumfahrt (DLR), Oberpfaffenhofen, Germany [c] Physical Oceanography Department, Centro de Investigación Científica y Educación Superior de Ensenada (CICESE), Ensenada, Mexico

Online publication date: 28 September 2010

To cite this Article Díaz Méndez, Guillermo M. , Lehner, Susanne , Ocampo-Torres, Francisco J. , Ming Li, Xiao and Brusch, Stephan(2010) 'Wind and wave observations off the south Pacific Coast of Mexico using TerraSAR-X imagery', International Journal of Remote Sensing, 31: 17, 4933 — 4955
To link to this Article: DOI: 10.1080/01431161.2010.485217
URL: http://dx.doi.org/10.1080/01431161.2010.485217

International Journal of Remote Sensing
Vol. 31, Nos. 17–18, September 2010, 4933–4955

Taylor & Francis
Taylor & Francis Group

Wind and wave observations off the south Pacific Coast of Mexico using TerraSAR-X imagery

GUILLERMO M. DÍAZ MÉNDEZ*†, SUSANNE LEHNER‡, FRANCISCO J. OCAMPO-TORRES§, XIAO MING LI‡ and STEPHAN BRUSCH‡

†Faculty of Marine Sciences, Universidad Autonoma de Baja California (UABC), Ensenada, Mexico

‡Remote Sensing Technology Institute, Deutsches Zentrum für Luft-und Raumfahrt (DLR), Oberpfaffenhofen, Germany

§Physical Oceanography Department, Centro de Investigación Científica y Educación Superior de Ensenada (CICESE), Ensenada, Mexico

High-resolution TerraSAR-X images are analysed for the first time to investigate the effects of gap winds on the sea surface off the south Pacific Coast of Mexico. StripMap and ScanSAR scenes were acquired over the Gulf of Tehuantepec on March 2008, coinciding with a strong *Tehuano* event with a wind speed of about 24 ms^{-1}. Although spatial variability of wind and wave parameters derived from the image analysis was fairly consistent with model data, Synthetic Aperture Radar (SAR)-derived wind speed was generally underestimated by 33%. The wave-retrieval algorithm, contrastingly, performed well enough to show evidence of shoaling and refracting ocean swell close to the shore. Furthermore, spatial evolution of image intensity spectral peaks suggests the presence of wave energy propagating to the SW, closely aligned with the offshore winds. Although further analyses are required, it could be the first time that growing waves in fetch-limited conditions have been detected through SAR remote sensing.

1. Introduction

On 15 June 2007, TerraSAR-X was successfully launched from Baikonur Cosmodrome, Kazakhstan, and acquired its first Synthetic Aperture Radar (SAR) image just four days later. Designed to orbit the Earth sun-synchronously at a nominal height of 514.8 km, it is the first of two Earth Observation (EO) satellites developed through a public-private partnership: the German Aerospace Centre and the European Aeronautical Defence and Space (EADS)-Astrium, respectively. The satellite is 4.9 m long, which is also the length of the SAR antenna, and has a diameter of 2.5 m. Its inclination is 97.44° with respect to the Earth's equator, and thus its revisit cycle is 11 days. The onboard SAR sensor emits radar pulses at a frequency of 9.65 GHz. TerraSAR-X's SAR has been designed to acquire images within four basic imaging modes: ScanSAR (SC), StripMap (SM), Spotlight (SL) and High Resolution Spotlight (HS). Table 1 summarizes their main characteristic parameters: while SM mode is the standard imaging mode of all, SC provides the largest coverage. SL and HS modes use phased array beam steering in the azimuth direction to increase the size of the synthetic aperture, which in turn, results in a higher azimuth resolution ρ_a at the

*Corresponding author. Email: gdiaz@uabc.mx

International Journal of Remote Sensing
ISSN 0143-1161 print/ISSN 1366-5901 online
http://www.tandf.co.uk/journals
DOI: 10.1080/01431161.2010.485217

Table 1. Characteristic parameters of TerraSAR-X basic imaging modes.

	Imaging modes			
	ScanSAR	StripMap	Spotlight	High-Resolution Spotlight
Swath width (km) (ground range)	100	30 sp; 15 dp	10	10
Product length (km) (ground range)	150	50	10	5
Incidence angle θ range (°)	20–45	20–45	20–55	20–55
Azimuth resolution ρ_a (m)	18.5	3.3 sp; 6.6 dp	1.7 sp; 3.4 dp	1.1 sp; 2.2 dp
Ground range resolution ρ_r (m)	1.70–3.49 ($\theta = 45$–$20°$)	1.70–3.49 ($\theta = 45$–$20°$)	1.48–3.49 ($\theta = 55$–$20°$)	1.48–3.49 ($\theta = 55$–$20°$)
Polarizations	single: HH or VV dual: HH/VV, HH/HV, VV/VH	single: HH or VV dual: HH/VV, HH/HV, VV/VH	single: HH or VV dual: HH/VV	single: HH or VV dual: HH/VV

sp = single polarization; dp = dual polarization.

cost of azimuth scene size. Additional information on TerraSAR-X's instrument, basic products and data structure can be found in Fritz and Eineder (2008).

Evaluation of atmospheric and oceanic processes through the analysis of SAR imagery is based on the principle that these phenomena modulate the distribution and behaviour of the capillary–gravity waves. Such waves are generated by the shear stress of the wind τ_w acting upon the sea surface; since very light winds suffice to generate these ripples, the latter are assumed to be omnipresent on the ocean surface. Capillary–gravity waves interact with the microwave pulses emitted by the SAR through Bragg resonance, the result of which is measured by the SAR antenna as the radar backscattered signal or image brightness. The wavelengths of the backscattering elements span 1–40 cm, and depend on the microwave frequency and its angle with respect to the vertical (i.e. incidence angle θ). Assembling or spreading of these ripples by increasing wind stress, tilting of the sea surface due to ocean swell, or converging/diverging of water masses for example, creates distinct patterns on the sea-surface roughness that can be imaged by SAR systems as spatial variations of the radar brightness. Given the fact that surface tension is the restoring force of capillary waves, natural or anthropogenic surfactants are also capable of modulating the radar backscatter from the ocean.

Assessments of the wind field and the sea state over large areas of the open ocean have been performed through the analysis of space-borne SAR under calm-weather conditions (Vesecky and Stewart 1982, Beal *et al*. 1983, 1986, Vachon and Dobson 1996) and extreme-weather conditions (Katsaros *et al*. 2002, Horstmann *et al*. 2006, Li *et al*. 2008, Reppucci *et al*. 2008), with promising results. SAR image analyses have delivered detailed information on the spatial variability of winds and waves in coastal areas (Johannessen *et al*. 1996, Ocampo-Torres 2001, Ocampo-Torres *et al*. 2007, Díaz Méndez *et al*. 2008). High-resolution wind maps derived from larger coverage SAR imagery are highly regarded by the wind farming industry because improved wind maps are desirable for resource assessment, offshore-site selection, etc. (Hasager *et al*. 2007, Brusch *et al.* 2008). SAR has become very important for the study of processes that are difficult to evaluate such as the interaction between ocean waves and sea-surface currents (Irvine and Tilley 1988, Ouchi 1994), formation and evolution of internal waves (Hwang *et al*. 2008) and the synoptic estimation of sea-surface circulation (Collard *et al*. 2008).

Hasselmann and Hasselmann (1991) derived a nonlinear integral transformation relation to describe the mapping of a two-dimensional ocean wave spectrum into a SAR image spectrum; an inversion of the proposed relation yielded the possibility of estimating the two-dimensional (2D) wave spectrum from any given SAR image spectrum. A few years later, additional inversion schemes were proposed to derive wave parameters from the few EO space-borne SAR sensors launched from 1978 onwards (Krogstad *et al.* 1994, Engen and Johnsen 1995, Hasselmann *et al.* 1996, Hasselmann *et al.* 1998, Mastenbroek and de Valk 2000). Improved algorithms (Schulz-Stellenfleth and Lehner 2004, Schulz-Stellenfleth *et al*. 2005, Collard *et al.* 2005) have been used by research institutions to derive sea-surface elevation, compute global statistics with either the full (or just the lower wavenumber part of the) wave spectrum, associated with the ocean swell, derived from the C-band SARs onboard the European satellites ERS-1, -2 and ENVISAT.

In this context, the X-band SAR mounted onboard TerraSAR-X has the potential to give new information on the sea surface because the nonlinearity and azimuthal cutoff described by Hasselmann and Hasselmann (1991) depend on the sensor's altitude. Given its relatively low flying orbit, TerraSAR-X is capable of observing features on

the sea surface not imaged by the L- nor C-band SAR sensors flying at approximately 800 km above sea level, like the above-mentioned European satellites, the Canadian Radarsat-1 and -2 and the Japanese Earth Resources satellite JERS-1 and the Advanced Land Observation Satellite ALOS. TerraSAR-X's imagery has thus been applied to ocean research right after the first scenes were available. Li *et al.* (2009) used Spotlight and StripMap scenes to analyse wave refraction and diffraction around Terceira Island at the Azores. Lehner (2008, personal communication) used SC, SM and SL mode scenes to derive high-resolution wind fields over the open ocean. Contrastingly, Brusch *et al.* (2010) took advantage of TerraSAR-X SAR's high spatial resolution to include them in ship surveillance and security applications.

The main objective of this study has been to investigate, through the analysis of high-resolution TerraSAR-X imagery, the detailed spatial evolution of the wind and wave fields during *Tehuano*-event conditions at the Gulf of Tehuantepec and adjacent Pacific Ocean. Evolution of the swell wave spectrum has been estimated by various authors through changes of spectral density (Ocampo-Torres 2001, Ardhuin *et al.* 2003), propagation direction and directional spreading (Beal *et al.* 1986, Ocampo-Torres and Vachon 2000, Ardhuin *et al.* 2003). Hence, our specific objectives included the assessment of the SAR image spectrum variability presumably induced by the strong gap winds, as well as an assessment of the spectral evolution and spatial variability of the fetch-limited wind-sea generated locally by the gap winds. It has also been of interest to investigate the spatial structure and variability of the wind field and general sea state during these strong-wind conditions.

The following sections include, first, a brief description of the *Tehuano* gap winds and their effect on the ocean surface off the south Pacific Coast of Mexico. This is followed by some theoretical background and by a short introduction on how the wind field and ocean waves were derived from the SAR images. Analysis results are presented and discussed in §4, while §5 includes a summary of findings.

2. Gap winds and their effect on the ocean surface

The Gulf of Tehuantepec located at the south Pacific Coast of Mexico, as well as the gulfs of Fonseca, Papagayo and Panama located in Central America (see figure 1(*a*)) are characterized by the occurrence of strong gap winds blowing off-shore into the Pacific Ocean during late autumn, winter and early spring months. According to Chelton *et al.* (2000), gap winds are the result of an atmospheric pressure gradient of up to 5 hPa between the Pacific and the Gulf of Mexico and western Caribbean, which forces up to three jets of wind through distinct low-elevation topographic discontinuities on the otherwise high mountain ranges. The resulting jets are usually colder and dryer than the surrounding Eastern Tropical Pacific air. Figure 1(*b*) shows an example of a triple gap wind event that occurred on 12 March 2008 at 06h Coordinated Universal Time (UTC) (source: European Centre for Medium-Range Weather Forecasts (ECMWF) blended QuikSCAT wind product; CERSAT 2002). The two southern jets have also been associated with funnelling of the trade winds through the mountain gaps in Nicaragua and Panama.

South-blowing gap winds occurring at the Gulf of Tehuantepec are locally known as *Tehuanos*. *Tehuano* events usually last from a few hours up to a few days, often reaching sustained velocities above 20 ms^{-1} and blowing as far south as 10° N latitude. Depending on duration and intensity, these events may induce a series of oceanographic phenomena, including strong offshore surface currents whose intensities have been

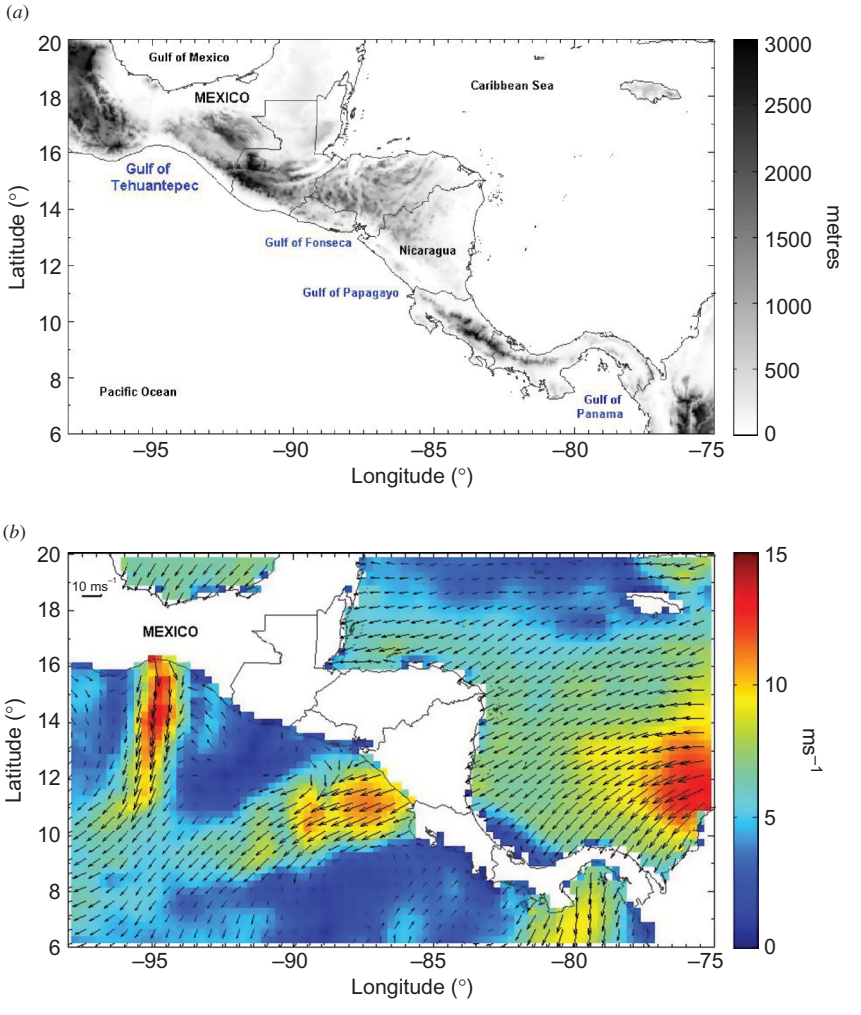

Figure 1. (*a*) Location of the gulfs of Tehuantepec, Fonseca, Papagayo and Panama in the Pacific Coast of Central America. Shades of grey represent topographic elevations in metres above sea level. (*b*) Example of a triple gap-wind event that occurred on 12 March 2008 at 06h UTC. Colour code is ms^{-1}. Source of wind data: ECMWF blended QuikSCAT wind product. Source of topographic data: NOAA- GGDC ETOPO-2 Global Gridded 2-minute Database.

measured as high as 1.5 ms^{-1} (Durazo 2009, personal communication), cooling of the sea-surface temperature, depression of the sea level of a few centimetres (Álvarez *et al.* 1989), as well as the generation of fetch-limited wind-sea propagating offshore (Ocampo-Torres *et al.* 2007, Díaz Méndez *et al.* 2008, García-Nava *et al.* 2009).

Figure 2 shows WAM (WAve Model; WAMDI 1988) results of wind-sea waves generated by persistent *Tehuanos* on 21 March 2008 at 00h UTC (model results provided by the German Weather Service, DWD). While shades of blue represent significant wave height H_s in metres, red arrows correspond to vectors of spectral peak wavelength L_p and its associated propagation direction α_p. Maximum computed values were $H_s = 5.1$ m and $L_p = 126.3$ m. According to the same source of data, wind speed at these location reached $U_{10} = 20.3$ ms^{-1}.

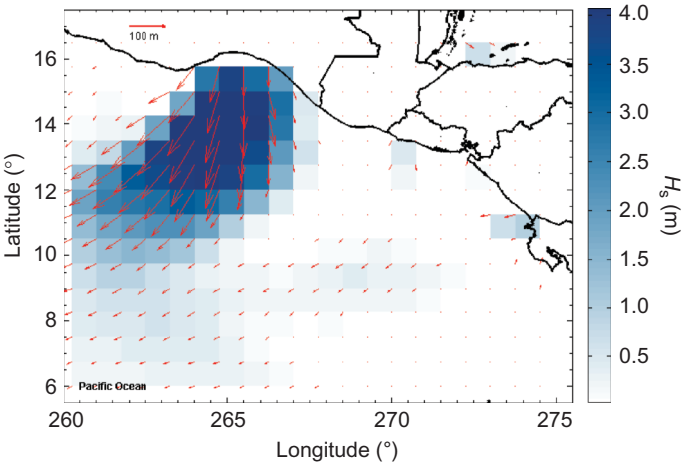

Figure 2. WAM results of wind-sea wave conditions at the Gulf of Tehuantepec and adjacent Pacific Ocean generated by the off-shore blowing gap winds on 21 March 2008 00h UTC: significant wave height H_s values in shades of blue; peak wavelength L_p and associated propagation direction α_p as red arrows. Source: DWD wind and wave data.

Strong *Tehuano* events are believed to induce variability on the evolution of the incoming waves generated by distant storms. Detailed analysis of the 2D wave spectra should provide evidence of ocean-swell variability due to refraction induced by surface currents, broadening or narrowing of the directional spreading and transfer of energy induced by the wind, particularly for larger swell wavenumbers. A number of authors (Snodgrass *et al.* 1966, Violante-Carvalho *et al.* 2004, Ardhuin and Jenkins 2005, 2006, Ardhuin *et al.* 2007) have considered the interaction between ocean swell and wind-sea propagating in opposite directions, and believe it may induce attenuation of the swell energy in deep waters.

3. Detection of wind and wave fields from TerraSAR-X imagery

3.1 *Theoretical background*

Estimation of the wind field within Deutsches Zentrum für Luft- und Raumfahrt (DLR)'s SeaSAR © Toolbox (DLR, Oberpfaffenhofen, Germany) is based on an empirical relation proposed by Masuko *et al.* (1986), who associated the normalized radar cross section (NRCS) σ_0 of a radiometrically calibrated SAR image to the wind speed 10 m above the sea surface U_{10}, the incidence angle of the radar beam θ and the azimuth angle φ between the wind direction and the SAR look direction. Depending also on polarization p and on the SAR wavelength λ, it is logarithmically expressed by:

$$\sigma_0(\lambda, p, U, \theta, \varphi) = 10[G(\lambda, p, \theta, \varphi) + H(\lambda, p, \theta, \varphi) \log_{10} U], \quad (1)$$

where σ_0 is given in dB. The values of G and H were found empirically and varied from –2.82 to –5.63 and from 1.62 to 2.82, respectively for a 10 GHz radar system with $\theta =$ 30°–60° and HH polarization, and from –2.76 to –4.59 and 1.54 to 2.48, respectively for VV polarization. The azimuth angle φ may be determined directly from the SAR imagery through Fast Fourier Transform (FFT) analysis or observation of wind streaks and other wind-induced processes on the sea surface, as well as input from external sources such as ship anemometers, spaceborne scatterometers or numerical models.

Similar to other geophysical model functions (GMFs), the X-MOD needs be inverted to derive U_{10} for given values of λ, p and θ. Following the CMOD4 (Stoffelen and Anderson 1997) and CMOD5 (Hersbach *et al.* 2004) algorithms derived for the C-band scatterometer onboard ERS-1, the X-band inversion is given by:

$$\sigma_0(U,\theta,\varphi) = x_0 + x_1 U + x_2 \sin(\theta) + x_3 \cos(2\varphi) + x_4 U \cos(2\varphi), \tag{2}$$

where x_n are coefficients tuned empirically from a set of 166 Spaceborne Imaging Radar- C/X-Band Synthetic Aperture Radar (SIR-C/X-SAR) and 52 TerraSAR-X images (Ren and Lehner 2008, personal communication).

Regarding the sea state, Schulz-Stellenfleth and Lehner (2004) described the SAR imaging of ocean waves as dominated by two mechanisms: the modulation of the NRCS by long waves (i.e. waves longer than the SAR resolution cell) through tilt and hydrodynamic processes in the ocean surface, and by Doppler shifts of the backscattered signal associated with the orbital motion of ocean waves. This latter mechanism is commonly referred to as velocity bunching. Tilt and hydrodynamic modulation of the NRCS, also called real aperture radar (RAR) modulation I^{RAR}, is a function of space $\boldsymbol{x}(x,y)$ and time t, and is usually described by a simple linear model such as

$$I^{\mathrm{RAR}}(\boldsymbol{x},t) = \frac{\sigma_0(x,t) - \langle\sigma_0\rangle}{\langle\sigma_0\rangle}, \tag{3}$$

where $\langle\sigma_0\rangle$ represents the ensemble-averaged value of the NRCS. Based on a Fourier representation of the ocean-surface elevation η at time t:

$$\eta(\boldsymbol{x},t) = 2\mathrm{Re}\left(\sum_k \eta_k \mathrm{e}^{\mathrm{i}(kx-\omega_k t)}\right), \tag{4}$$

where Re denotes the real part of the Fourier transform, $\boldsymbol{k}$ is the wavenumber vector, $\eta_{\boldsymbol{k}}$ are the complex Fourier coefficients of the sea surface and $\omega_{\boldsymbol{k}}$ is the angular wave frequency that is associated with $\boldsymbol{k}$ through the so-called dispersion relation. By combining equations (4) and (3), I^{RAR} can be rewritten as:

$$I^{\mathrm{RAR}}(\boldsymbol{x},t) = 2\mathrm{Re}\left(\sum_k T_k^{\mathrm{RAR}} \eta_k \mathrm{e}^{\mathrm{i}(kx-\omega_k t)}\right), \tag{5}$$

where $T_{\boldsymbol{k}}{}^{\mathrm{RAR}}$ is the RAR modulation transfer function (MTF). As noted by these authors, there is still some uncertainty on the exact phase and magnitude of the RAR MTF.

SAR imaging processes uses the phase history of the radar backscattered signal, distorted by the Doppler shifts induced by the wave motions, to synthesize the resolution in the azimuth direction. Since the ocean surface is not stationary, a slant range component of the average orbital velocity u_{r} during the SAR integration time (usually 1 s), causes shifting ξ of the respective image point in the azimuth direction. This shifting equals the distance from the SAR antenna to the ocean target or slant range R times u_{r} divided by the satellite velocity V. In a linear approximation, u_{r} can be expressed in terms of the wave spectrum as:

$$u_{\mathrm{r}}(\boldsymbol{x},t) = 2\mathrm{Re}\left(\sum_k T_k^{\mathrm{u}} \eta_k \mathrm{e}^{\mathrm{i}(kx-\omega_k t)}\right), \tag{6}$$

where $T_{\boldsymbol{k}}{}^{\mathrm{u}}$ is the orbital velocity transfer function given by:

$$T_k^{\mathrm{u}} = -\omega_k \left(\frac{k_y}{|\boldsymbol{k}|} \sin\theta + \mathrm{i}\cos\theta \right), \tag{7}$$

and k_y is the wavenumber in the azimuth direction. Based on equations (5) and (7), the following integral expression can be derived for a SAR image MTF I^{SAR} of a moving sea surface:

$$I^{\mathrm{SAR}}(\mathbf{x}) = \frac{\sqrt{\pi}}{2\rho_{\mathrm{a}}} \int (1 + I^{\mathrm{RAR}}(\boldsymbol{x}')) \mathrm{e}^{-\frac{\pi^2}{4\rho_{\mathrm{a}}^2}(x - x' - \xi(x'))^2} \delta(y' - y) \mathrm{d}x' \mathrm{d}y' - 1. \tag{8}$$

Here, $\boldsymbol{x}(x, y)$ and $\boldsymbol{x}'(x', y')$ denote the coordinates of the image in the Cartesian and the ocean planes, respectively.

3.2 *Data*

More than a dozen scenes have been acquired so far by the TerraSAR-X over the Gulf of Tehuantepec. In this paper, however, we present results from the two that coincide with the occurrence of a strong *Tehuano* event. This small dataset included a higher resolution SM scene from 20 March 2008 at 12:19h UTC and a larger coverage SC acquired 12 hours later. Characteristics of these two scenes are summarized in table 2; their location and extent are shown on a map in figure 3. This map also shows bathymetric contours at the Gulf of Tehuantepec and the adjacent Pacific Ocean.

Table 2. Characteristics of the two TerraSAR-X images analysed in this study.

Imaging mode	Date and time (UTC)	Path	Track azimuth	Polarization	Coverage (km)
StripMap	20 March 2008 @ 12:19h	Descending	348.6°	HH	30 × 50
ScanSAR	21 March 2008 @ 00:19h	Ascending	191.4°	HH	100 × 150

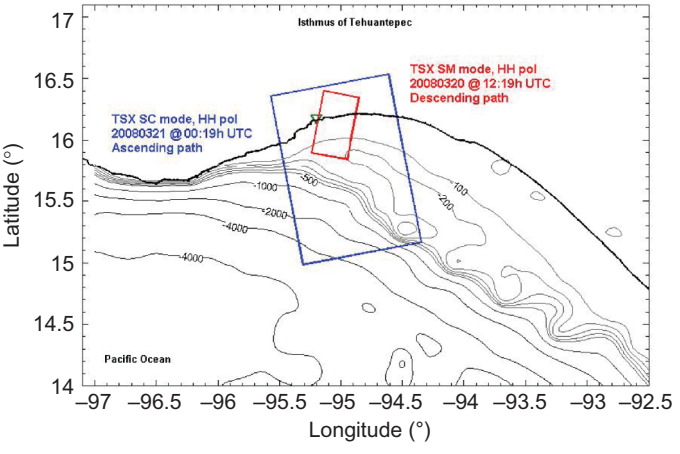

Figure 3. Location and extent of the two TerraSAR-X images analysed in this study. The red rectangle depicts the perimeter of the SM scene acquired on 20 March 2008 at 12:19h UTC; the blue rectangle depicts the perimeter of the SC acquired on 21 March. The small green triangle marks the location of the Port of Salina Cruz. Also shown are bathymetric contours from the Gulf of Tehuantepec and the adjacent Pacific Ocean.

3.3 *Method*

As mentioned above, estimation of the wind field from TerraSAR-X imagery was based on the X-MOD GMF. While values of θ are given for each pixel on the image annotation file, the azimuth direction ϕ was derived by visual observation of wind streaks and other distinct patterns directly on the image quicklooks; according to Reppucci *et al*. (2008), they tend to align fairly well with the direction of the wind. In their paper, these authors present a flow chart depicting the steps followed to calculate the wind speed using the CMOD5 GMF. In our case, we followed similar steps, but applied the X-MOD instead.

Ocean-wave conditions were derived through the analysis of SAR image intensity spectra since no inversion algorithm has been yet proposed nor validated for the TerraSAR-X SAR. A mosaic of spectra was computed from each scene and its corresponding peak wavenumber k_p was calculated following the steps depicted in the flow chart included in figure 4.

Within the SeaSAR Toolbox, a given image is first read and its corresponding quicklook is created. Before it is processed for wind or waves, the scene is calibrated and, if appropriate, a land mask is applied. A value for sub-image size is input by the

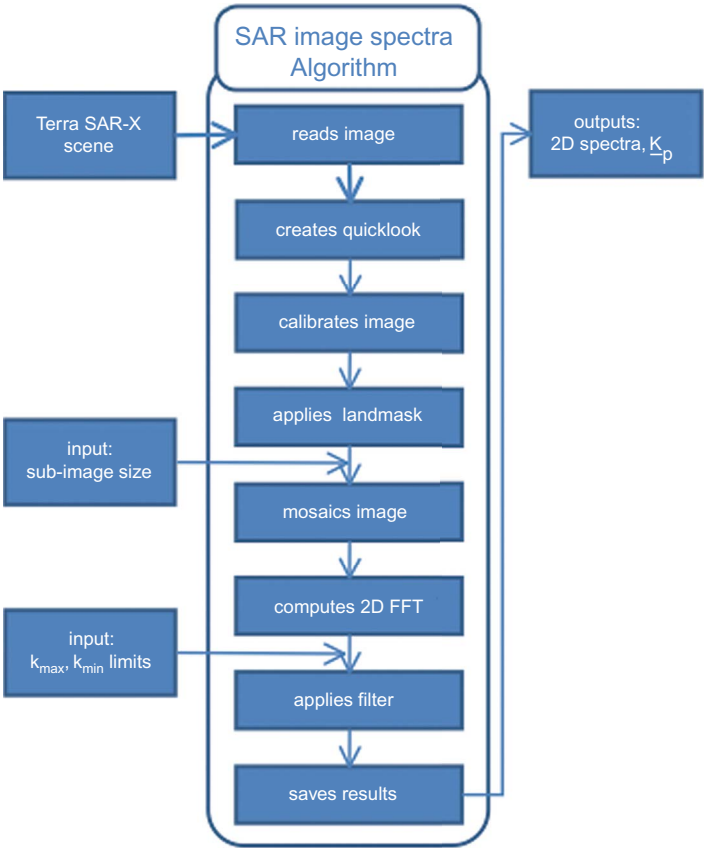

Figure 4. Flow chart of the algorithm followed by the SeaSAR toolbox to compute the two-dimensional SAR image intensity spectrum and its corresponding peak wavenumber k_p.

user and the image is tiled accordingly. A 2D FFT is performed on each sub-image; the result is filtered using maximum and minimum wavenumber limits, usually $k_{max} = 0.09$ rad m^{-1} and $k_{min} = 0.01$ rad m^{-1}, respectively, which roughly correspond to ocean waves with deep-water wavelengths $L_{min} = 70$ m and $L_{max} = 600$ m, respectively. These limits however, can be conveniently modified by the user. The resulting matrix is then stored for post-processing, plotting and estimation of k_p. It is worth mentioning that, for our analyses, the wavenumber limits were set to $k_{max} = 0.063$ rad m^{-1} and $k_{min} = 0.02$ rad m^{-1} for the SM scene and $k_{max} = 0.04$ rad m^{-1} and $k_{min} = 0.01$ rad m^{-1} for the SC, which correspond to shoaling waves with wave periods T of the order of 8–14 s in the first case and $T = 10$–20 s in the second, typical for ocean swell.

4. Results and discussions

According to ECMWF blended QuikSCAT wind data (CERSAT 2002), a strong gap wind event developed at the Gulf of Tehuantepec late on 19 March 2008. Figure 5 shows a time series plot of wind speed U_{10} extracted from this dataset at three locations: P1 (16.125° N, 94.875° W), P2 (15.375° N, 95.125° W) and P3 (14.625° N, 95.375° W), located approximately 10, 100 and 185 km offshore (along the wind-jet axis), respectively. As can be seen on the graph, the *Tehuano* event quickly intensified, reaching velocities of up to 23 ms^{-1} about 100 km offshore (point P3) on 20 March. Contrastingly, closer to the shore (P1), wind-speed variability was less pronounced. The *Tehuano* decreased down to 5 ms^{-1} late on 21 March before intensifying again the next day. By noon, it reached a second intensity peak, registering wind-speed values above 10 ms^{-1}. The vertical arrows in figure 5 represent the times of acquisition of the two analysed TerraSAR-X images, which as can be noted, correspond to the period of stronger winds. Wind-speed values derived from the 21 March ScanSAR scene, collocated to locations P1 and P2, are included for comparison.

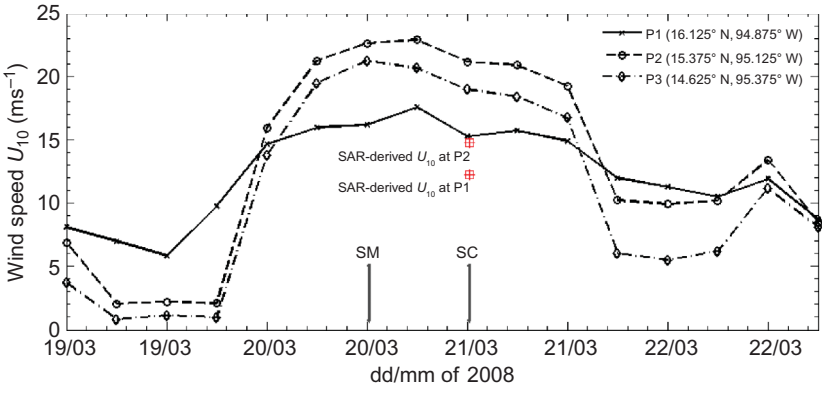

Figure 5. Time series of wind speed U_{10} during the 19–22 March 2008 *Tehuano* event. Points P1, P2 and P3 are located ca. 10 km, 100 km and 185 km away from the shore along the wind-jet axis, respectively (source: ECMWF blended QuikSCAT wind data; CERSAT 2009). The vertical arrows indicate the time of acquisition of the two analysed TerraSAR-X images; red squares indicate wind speed collocated to points P1 and P2 derived from the 21 March 2008 ScanSAR scene.

4.1 *SAR-derived wind and wave parameters*

Conspicuous wind streaks and other wind-related features of various scales were appreciated by visual inspection on both TerraSAR-X images (figures 6 and 7). Alternating bright and dark patterns extending perpendicular to the shore were observed on the ocean surface as well as on Tehuantepec's coastal lagoons. Larger scale oscillations, presumably atmospheric gravity waves, were observed on the SC scene, apparently propagating perpendicular to the shore.

All these features were used to carefully derive the wind direction α and its angle ϕ with respect to the SAR look direction ψ, required by the X-MOD GMF in order to solve for the wind speed. Once this has been input in the Toolbox, vector fields of wind speed and direction were constructed. Figure 6 shows a map of the estimated wind

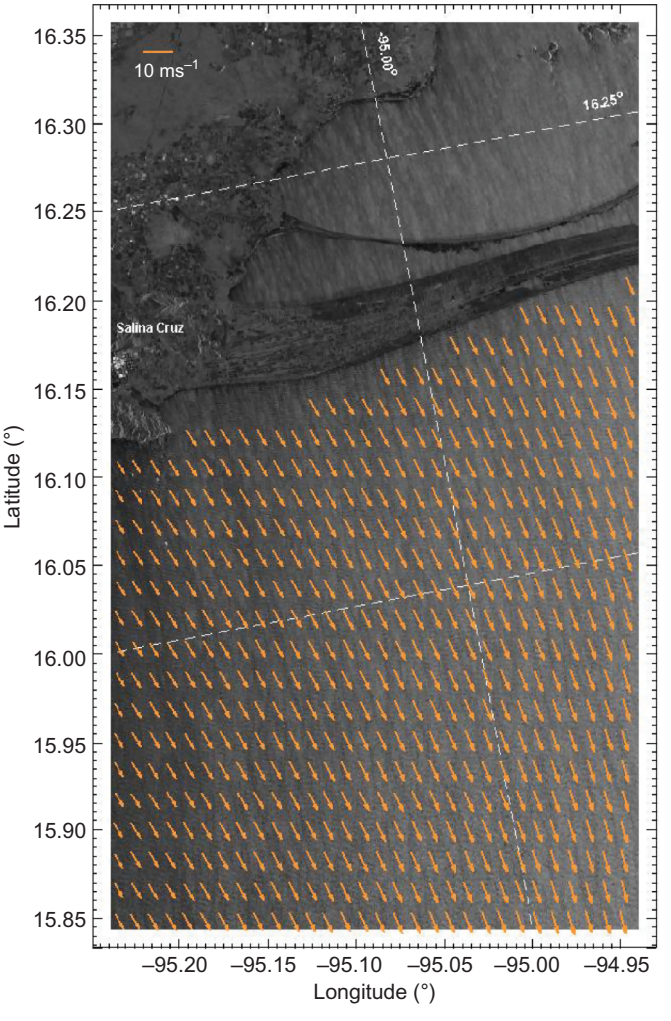

Figure 6. Wind field at the Gulf of Tehuantepec during a strong *Tehuano* event derived from the SM scene acquired on 20 March 2008 at 12:19h UTC. Meridians and Parallels shown as dashed lines.

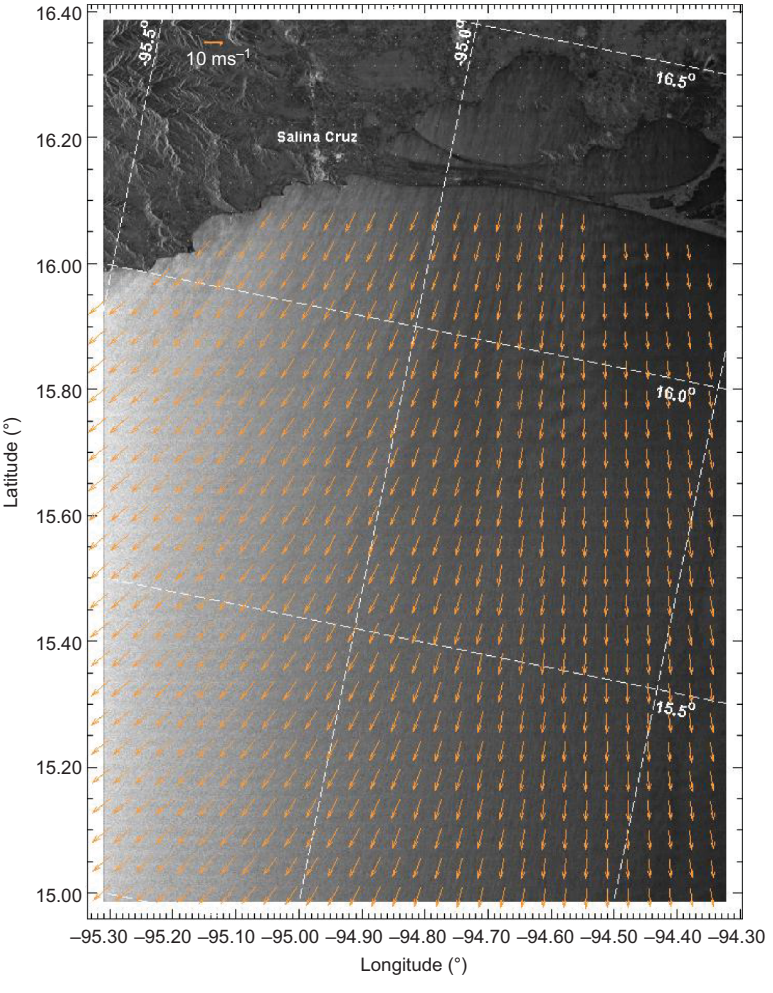

Figure 7. Similar to figure 6: wind vectors derived from the SC scene acquired on 21 March 2008 at 00:19h UTC.

field overlaid on top of a quicklook from the 20 March SM scene. The SAR quicklook is oriented according to the platform flight direction and thus, it points to the top of the page; Meridians and Parallels are shown as dashed lines. Looking carefully, it can be noted that the wind was strongest towards the core of the jet, which laid to the right of the scene; but it also increased away from the coast. SAR-derived wind-speed values retrieved by the X-MOD algorithm range from $U_{10} = 10.5$ ms^{-1} at the left end of the scene to $U_{10} = 15.0$ ms^{-1} on the right, and from $U_{10} = 8.4$ ms^{-1} just off-shore from the port of Salina Cruz to $U_{10} = 15.2$ ms^{-1}, 42 km to the southeast. Average wind speed estimated for this scene was $U_{10} = 13.3$ ms^{-1}. Similarly, figure 7 shows the wind retrieved from the SC image acquired on 21 March. This larger coverage scene (see table 2) renders a better detail of the fan-shaped spatial distribution of the wind field in the area as described by Chelton *et al.* (2000). It is interesting to observe that the wind streaks on the ocean surface are oriented to the south–southwest, contrasting to those in figure 6, which lay to the south–southeast. This suggests the rotation of the

wind-jet axis as the *Tehuano* event progresses. Because a larger extent of the wind jet is covered by this SC scene, corresponding wind-speed statistics are slightly higher than those estimated from the SM scene: in this case, the higher values are located to the left of the figure and range from $U_{10} = 10.4$–16 ms^{-1}, with average $U_{10} = 13.8$ ms^{-1}.

SAR-derived wind values, however, were relatively lower than collocated grid points from the blended QuikSCAT wind data of figure 5. The latter range from $U_{10} = 18.8$–21 ms^{-1} for 20 March and 10–21.1 m s^{-1} for 21 March, with averages of 20 ms^{-1} and 16.8 ms^{-1}, respectively, at the areas covered by the SAR images. According to Ren and Lehner (2008, personal communication), the X-MOD algorithm implemented in the Toolbox has been tuned with a limited number of strong-wind cases and thus, this could be one reason for the underestimation of wind-speed values. Another important cause may be that the X-MOD algorithm was tuned for VV polarization images, and both scenes analysed on this study are HH polarized, which is known to produce weaker backscatter. As discussed by Horstmann *et al.* (2000), additional sources of error include the dependence of the NRCS on the radiometric accuracy of the SAR product, which led to large errors on wind speed, particularly in the case of high wind speeds and small incidence angles. Furthermore, Donelan and Pierson (1987) found that for high wind speeds, σ_0 becomes less sensitive to the wind speed and then decreases as the wind speed increases.

Underlying all the above-mentioned wind-related features, a distinct pattern of shorter wavelength texture associated with ocean waves was observed on the images. Due to its higher resolution, it was particularly evident on the SM scene where at least two sets of wavy features, presumably two ocean-swell systems with different propagation direction, crossed each other and eventually aligned close to the shore. Figure 8(*a*) shows a map with results from the SeaSAR Toolbox's wave-detection algorithm overlaid on the 20 March 2008 SM scene.

As can be seen in the figure, most of the double-headed vectors representing the wavelength L_p and ambiguous propagation direction α_p of the ocean waves have a quasi-northerly orientation. It was not possible to perform the 180° ambiguity discrimination due to the fact that the scenes were not acquired in complex mode, and thus, no information on the phase of the scatters was available. Nevertheless, given their magnitude and proximity to the coast, it was not difficult to infer that propagation direction was towards the coast. The progressive shortening of the vectors from the bottom of the scene towards the shore represents a decrease in wavelength from approximately $L_p = 330$ m down to about $L_p = 190$ m. The latter, along with the shifting in propagation direction α_p, is presumably accounted for by the combined phenomena of wave refraction and shoaling due to decreasing water depth towards the coast. Indeed, as can be seen in figures 3 and 8(*a*), the water depth at the southern end of the SM scene reaches 200 m, and decreases gently towards the shore.

Figures 8(*b*)-(*d*) show a set of 2D SAR image intensity spectra calculated from the three ca. 5 × 5 km (2048 × 2048 pixels) sub-images shown as red squares in figure 8(*a*). Horizontal and vertical axes are range and azimuth wavenumbers k_x and k_y, respectively, in rad m^{-1}. Colour coding on these plots represents normalized values of image intensity from the 2D FFT, which may be associated with the energy of the ocean waves as suggested by Alpers *et al.* (1981) through

$$S(\boldsymbol{k}) = \frac{S_I(\boldsymbol{k})}{\left(\boldsymbol{I}^{SAR}(\boldsymbol{k})\right)^2}, \tag{8}$$

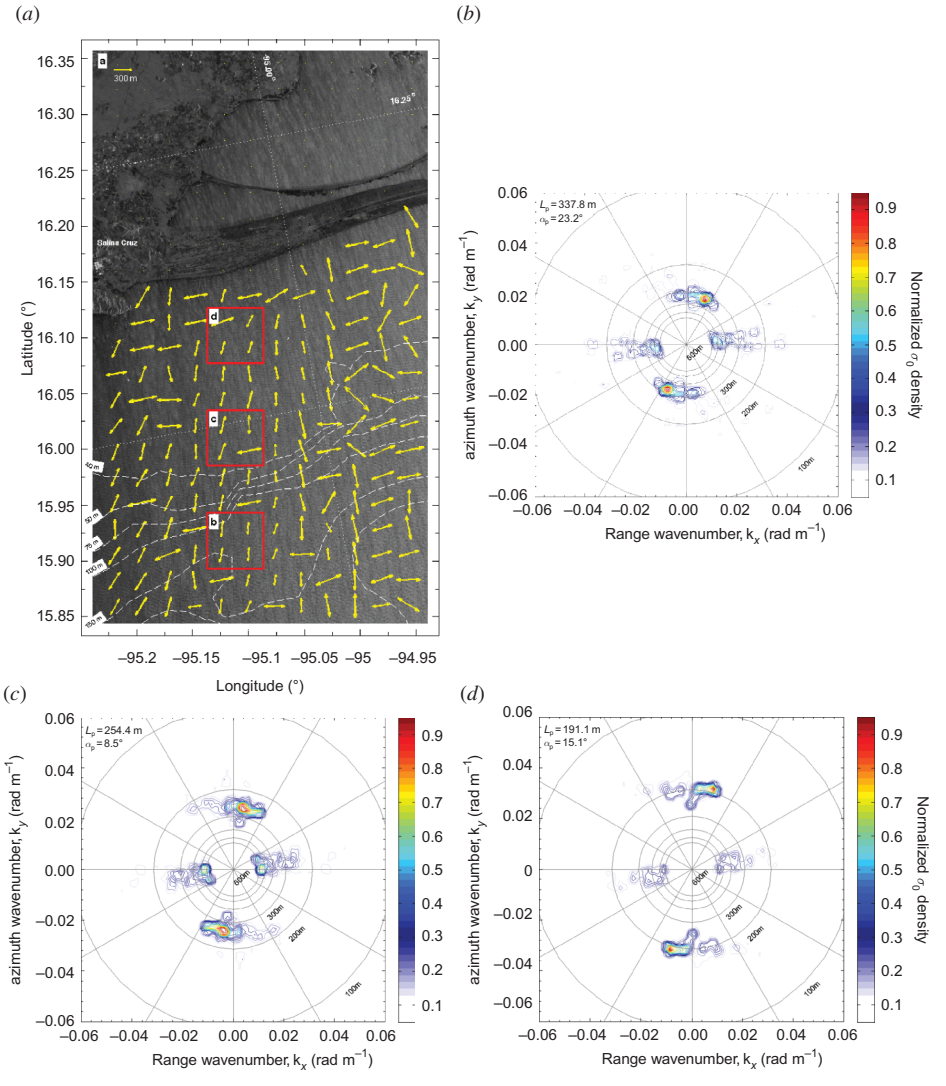

Figure 8. Ocean-wave conditions during a strong *Tehuano* event derived from the SM scene acquired on 20 March 2008. (*a*) Estimated SAR-image peak wavelength L_p in yellow; two-head arrows represent wave propagation direction with 180° ambiguity. Meridians and Parallels shown as dashed lines; bathymetric contours above 40 m of water depth shown as solid white lines. (*b*)–(*d*) Two-dimensional SAR-image intensity spectra calculated from the three ca. 5 × 5 km sub-images shown as red squares on (*a*); (*d*) is closer to the shore. Horizontal and vertical axes are range and azimuth wavenumbers, k_x and k_y respectively, in rad m^{-1}.

where $S(\boldsymbol{k})$ is the ocean wave spectrum as a function of wavenumber $\boldsymbol{k}$, $S_I(\boldsymbol{k})$ is the intensity spectrum of the SAR image and $I^{SAR}(\boldsymbol{k})$ is the SAR MTF corresponding to a linear mapping of the ocean surface. As can be observed on these spectra, a series of high-intensity peaks was estimated by the SeaSAR algorithm. While peaks closely aligned with the horizontal axis ($k_y \approx 0$, $k_x \approx \pm\, 0.012$ rad m^{-1}) were associated with sea-surface roughness patterns induced by the wind, those located close to the vertical

axis ($k_y \approx \pm$ 0.02–0.035 rad m^{-1}, $k_x \approx 0$) are believed to be associated with the ocean swell. Phenomena of wave refraction and shoaling mentioned above were also noted on these spectra, as the latter peaks shifted from close to the $L = 300$ m past the $L =$ 200 m contours, closer to the shore. Overall shift from these peaks from $L_p = 337.8$ m in figure 8(*b*) to $L_p = 191.1$ m in figure 8(*d*) ($k_p = 0.018$ rad m^{-1} to $k_p = 0.032$ rad m^{-1}) represent a wavelength decrease of ca. 45% and change in propagation direction of 8° ($\alpha_p = 23.2$–$15.1°$).

A similar type of analysis was applied to the SC scene from 21 March 2008. Figure 9 shows the results for 1024 × 1024 pixel sub-images. A wavelength filter was set to detect intensity peaks within $L = 70$–600 m, which approximately correspond to wave periods of $T \approx 7$–20 s, typical for ocean swell. Arrows on the left half of the scene represent wavelengths of the order of $L_p = 250$ m, and are consistent in orientation and length with the incoming swell from the WAM results described in §2. Figures 9(*b*)-(*d*) show 2D SAR image spectra calculated for the ca. 17 × 17 km (2048 × 2048 pixels) sub-images shown as red squares in figure 9(*a*). Though one can hardly appreciate shoaling and refraction of the peaks associated with the swell waves on these spectra ($L_p \geq 300$ m), shifting of those located outside the $L = 200$ m contour ($k_x = k_y = 0.031$ rad m^{-1}) is far more noticeable.

These secondary peaks with relatively higher wavenumbers ($k_{p\text{-}b} = 0.061$ rad m^{-1}, $k_{p\text{-}c} = 0.063$ rad m^{-1} and $k_{p\text{-}d} = 0.073$ rad m^{-1}, whose corresponding wavelengths are $L_{p\text{-}b} = 103$ m, $L_{p\text{-}c} = 99.5$ m and $L_{p\text{-}d} = 85.5$ m; subscripts *b–d* refer to the SAR spectra from figure 9(*b–d*)), which decrease away from the shore (L_p increases) and thus could not be associated with the incoming ocean swell. Based on its wavelength range and increase with distance, we believe that these SAR image intensity peaks could be associated with the fetch-limited wind-sea waves generated by the *Tehuano* winds. These results deserved, nonetheless, further investigation.

4.2 *Comparison to parametric relations*

In order to examine whether or not the intensity peaks detected on the image spectra shown in figures 9(*b*)–(*d*) could correspond to the growing wind-sea waves, our results were contrasted with the parametric wave-prediction relations proposed by Kahma and Calkoen (1992). Figure 10 shows a plot of peak period T_p as a function of fetch X for the case of stable stratification that, according to García-Nava *et al.* (2009), dominate during *Tehuano* events. Curves of wave growth are plotted for wind-speed values $U_{10} = 5$–30 m s^{-1} every 5 m s^{-1}.

Asterisks indicate the peak periods $T_p = 8.1$, 7.9 and 7.4 s derived, respectively, from the wavelengths $L_{p\text{-}(b\text{–}d)}$ described above through the deep-water dispersion relation. The associated fetches $X_{b\text{–}d} = 122.6$, 91.8 and 57.8 km represent the distances measured from the shore to the centre of the red squares in figure 9(*a*), closely following the direction of the wind. For comparison, triangles correspond to peak period values calculated directly through Kahma and Calkoen's (1992) relations at fetches $X_{b\text{–}d}$ with collocated wind-speed values $U_{10\text{-}b\text{–}d} = 15.4$, 16.03 and 17.9 ms^{-1}, obtained from the blended QuikSCAT data. Note that predicted values $T_{p\text{-}b}' = 6.8$ s, $T_{p\text{-}c}' = 6$ s, $T_{p\text{-}d}' = 5.3$ s are about 15–30% lower than those derived from the TerraSAR-X images. Corresponding predicted wavelengths, $L_{p\text{-}b\text{–}d}' = 73.8$ m, 57.3 m and 44.1 m are thus shorter than measured $L_{p\text{-}b\text{–}d}$ values. Table 3 summarizes these values.

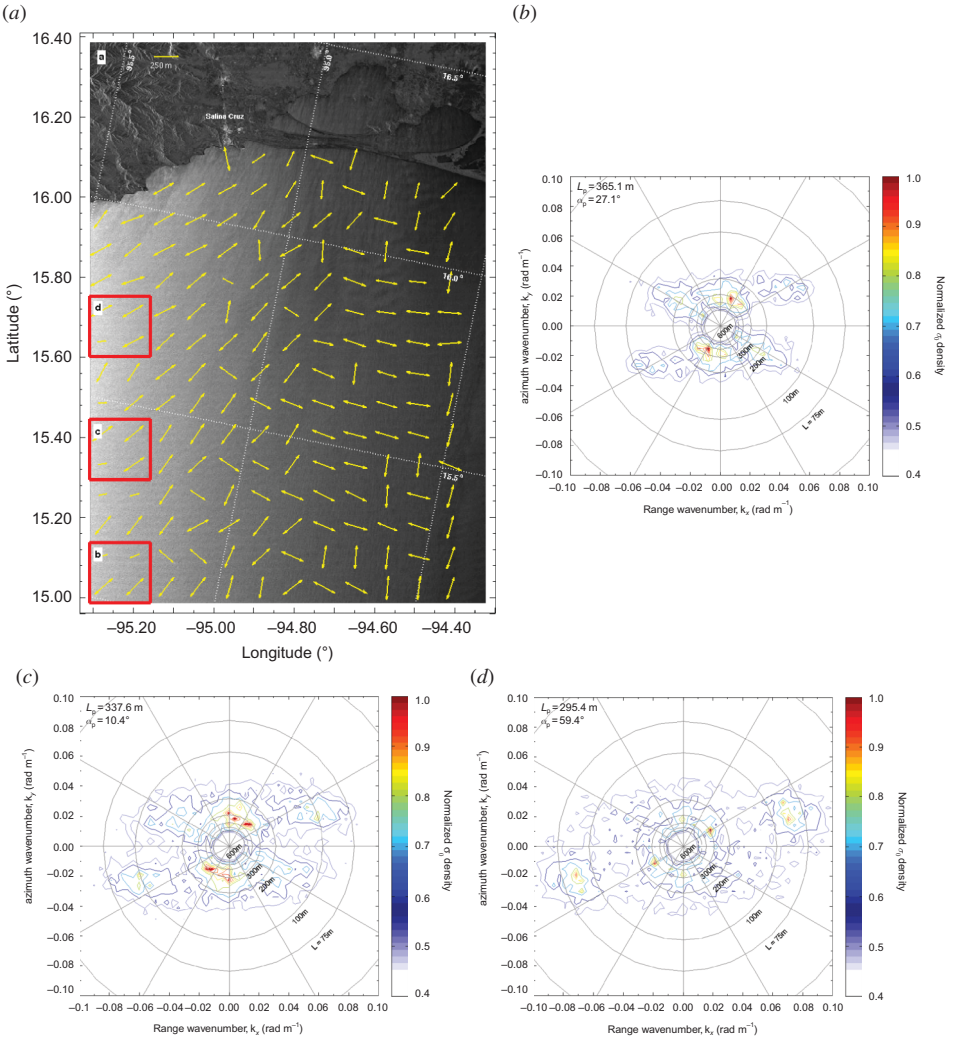

Figure 9. Similar to figure 8, ocean-wave conditions derived from the SC scene acquired on 21 March 2008. (*a*) Estimated SAR-image peak wavelength L_p in yellow; two-head arrows represent wave propagation direction with 180° ambiguity. Meridians and Parallels shown as dashed lines; bathymetric contours above 40 m of water depth shown as solid white lines. (*b*)–(*d*) two-dimensional SAR image intensity spectra calculated from the three ca. 17 ×17 km sub-images shown as red squares on (*a*); (*d*) is closer to the shore. Horizontal and vertical axes are range and azimuth wavenumbers, k_x and k_y respectively, in rad m^{-1}.

One of the several possible reasons for the differences between SAR-derived and parametric-predicted wave parameters is the fact that the wave-growth relations have been postulated for a straight shoreline perpendicular to the wind direction. This is not the case at Tehuantepec where the wind-jet axis is oblique with respect to the shore and rotates during the evolution of the *Tehuano* event. Other reasons, as underlined by Kahma and Calkoen (1992), include gustiness and variations of surface roughness and air/sea temperature. Although we are inclined to consider that deviations from

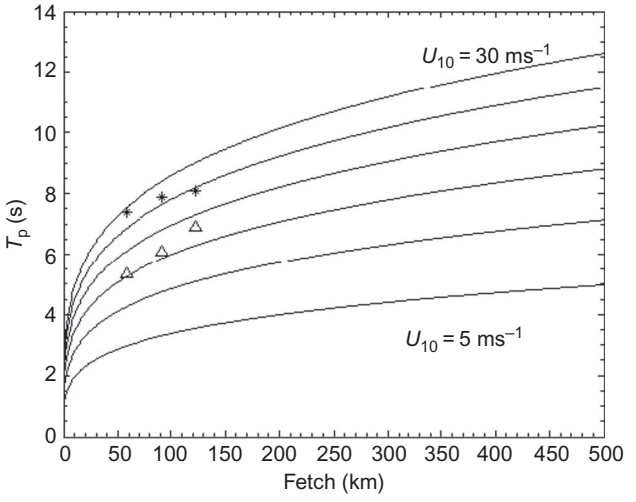

Figure 10. Fetch-limited wave growth derived from parametric prediction relations proposed by Kahma and Calkoen (1992) for the case of stable stratification: peak period T_p as a function of fetch. Solid curves correspond to wind speed U_{10} = 5–30 ms^{-1} every 5 ms^{-1}. Asterisks correspond to the three cases derived from the SAR image intensity spectra; for comparison, triangles correspond to values calculated through these parametric relations for the appropriate fetch and wind speed.

Table 3. Comparison of SAR-derived wave parameters, parameters estimated through the relations of Kahma and Calkoen (1992) and the collocated DWD data. Subscripts *b–d* refer to the SAR spectra from figures 9(*b*)–(*d*); fetch X was directly estimated from the images; wind speed U_{10} was retrieved from the blended QuikSCAT wind product.

			SAR-derived		Parametric relations			DWD data	
	X (km)	U_{10} (ms^{-1})	L_p (m)	T_p (s)	L_p' (m)	T_p' (s)	H_s' (m)	H_s (m)	α_p (°)
b	122.6	15.4	103.0	8.1	73.8	6.8	3.0	4.9	255
c	91.8	16.0	99.5	7.9	57.3	6.0	2.3	4.6	254
d	57.8	17.9	85.5	7.4	44.1	5.3	1.8	3.9	254

parametric relations may be due to the modulation of the growing wind-sea by the incoming ocean swell, as suggested by García-Nava *et al.* (2009), our research still awaits the evidence to adequately support such a hypothesis.

4.3 *Linearity analysis*

Another explanation for these discrepancies may arguably be that the formation of the SAR image is highly nonlinear, and thus a wave-inversion scheme is required to properly derive wave parameters. In order to further explore this idea, we have compiled wind and wave model data from the vicinity of the SAR wave-retrieval results of figures 9(*b*)–(*d*) and plotted them on a linearity boundary graph following Alpers *et al.* (1981, figure 8). A condition that has to be fulfilled for azimuth travelling waves to be imaged linearly, i.e. to have a constructive velocity bunching MTF R^{bunch}, is

$$\left|\frac{R}{V}\frac{\partial u_r}{\partial x}\right| << 1. \tag{9}$$

Equation (9) may be expressed in terms of ocean-swell and satellite parameters by

$$\left|\frac{R}{V}\frac{\partial u_r}{\partial x}\right| \leq \frac{R}{V}\frac{H}{2}|\boldsymbol{k}|\omega_k G\cos\Phi \equiv C, \tag{10}$$

where H is the wave height or twice the wave amplitude, $|\boldsymbol{k}|$ is the modulus of the wavenumber vector, Φ is the angle between the platform flight direction and the wave propagation direction α_p and

$$G(\Phi,\theta) = \sqrt{\sin^2\theta\sin^2\Phi + \cos^2\theta} \tag{11}$$

is called the geometric parameter. $|C| = 0.3$ is mentioned to be a reasonable choice for the linearity limit, where the mapping turns from linear (below each corresponding curve in figure 11) to nonlinear (above).

According to the DWD data for the Gulf of Tehuantepec on 21 March 2008 at 00h UTC, H_s values from both sea and swell are of the same order of magnitude: mean $H_{s\text{-}sea} = 2.6$ m and mean $H_{s\text{-}swell} = 3.7$ m. These values span $H_{s\text{-}swell} = 0.5$–5.3 m and $H_{s\text{-}sea} = 0.2$–5.1 m, respectively. Model H_s values interpolated and collocated to the image intensity spectra of figures 9(*b*)–(*d*) (DWD grid points were located 10 to 15 km away from the centres of the sub-images) were $H_{s\text{-}sea\text{-}b\text{–}d} = 4.9$, 4.6 and 3.9 m, respectively. Hence, propagation direction values relative to north varied from $\alpha_{b\text{–}d} = 255$ to 254.6 and 254°, respectively. Satellite parameters used in equation (11) to construct figure 11 are $V_{TSX} = 7.6\,\text{km s}^{-1}$, $\theta_{TSX} = 25°$, heading = 348.6° (ascending path), platform height $h_{plat} = 514.8$ km and $R_{TSX} = h_{plat} / \cos\theta_{TSX}$ for TerraSAR-X. For comparison, linearity boundaries for the Advanced Synthetic Aperture Radar (ASAR) carried onboard ENVISAT have also been derived. ENVISAT's parameters are: $V_{ENV} = 7.55\,\text{km s}^{-1}$, $\theta_{ENV} = 22°$, heading = 347.9°, platform height $h_{plat} = 800$ km and $R_{ENV} = h_{plat}/\cos\theta_{ENV}$.

It is not surprising to observe in figure 11 that TerraSAR-X linearity boundaries (thick solid and dashed lines) allow for a relatively larger linear regime than ENVISAT (thin lines). It is worth noting that curves corresponding to the case where $\Phi \neq 0$ for both platforms have a relatively higher slope due to the fact that the wind-sea waves generated by the *Tehuano* propagate are almost perpendicular to the azimuth direction. While asterisks represent the location of waves with wavelengths L_p derived from the SAR image analyses and significant wave height H_s interpolated from the DWD wave-model data, triangles represent predicted wave parameters $L_{p\text{-}b\text{–}d}'$ and $H_{s\text{-}b\text{–}d}'$ estimated through the parametric relations of Kahma and Calkoen (1992) (see §4.2).

The latter cases are located in the nonlinear regime; contrastingly, squares found on TerraSAR-X's linear regime represent the case of L_p derived from the SAR analysis and the corresponding predicted parametric $H_{s\text{-}b\text{–}d}'$, which, as noted in table 3, are almost half the model H_s values. Steeper waves are thus likely to lie in the nonlinear regime and hence, are not correctly imaged by the SAR.

Since two out of three cases lie on the nonlinear regime close to the boundary, it is arguable whether or not an inversion scheme should be applied to properly derive fetch-limited wave parameters under such strong wind cases. Though not presented here, similar results obtained for the swell waves from the DWD data provided additional evidence to suggest that a wave-inversion scheme is desirable.

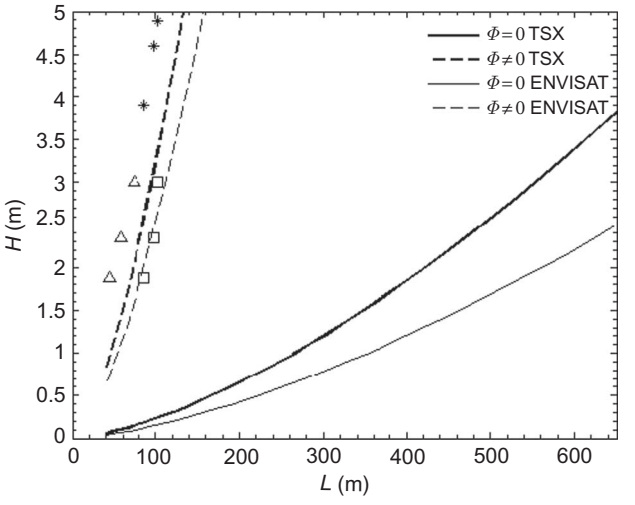

Figure 11. Regions where the velocity bunching modulation transfer function, R^{bunch}, changes from linear to nonlinear (below and above the curves, respectively; after Alpers *et al.* (1981)). Thick lines are for the TerraSAR-X platform with an incidence angle $\theta = 25°$; thin lines are for the ENVISAT satellite with an incidence angle $\theta = 22°$. Solid lines represent the case of waves propagating parallel to the satellite flight direction, $\Phi = 0$; dashed lines are for waves travelling at an angle, $\Phi \neq 0$, with respect to the satellite track. Asterisks represent a case with L_p derived from the SAR analyses and H_s interpolated from DWD wave-model data; triangles are for a case where L_p' and H_s' were estimated through the parametric relations of Kahma and Calkoen (1992); squares are for the composite of L_p derived from SAR data and H_s' calculated from the parametric relations.

5. Conclusions

The results shown and discussed in this paper are examples of the great potential that high-resolution TerraSAR-X images have for revealing the detailed spatial evolution of the ocean surface. Synoptic wind and wave conditions at the Gulf of Tehuantepec and the adjacent Pacific Ocean during a strong *Tehuano* event were estimated from a 30 × 50 km SM scene, as well as from a larger 100 × 150 km SC scene acquired on 20 and 21 March and 2008 at 12:19h and 00:19h UTC, respectively. Wind retrieval based on the X-MOD algorithm reported a fan-shaped distribution of the wind with the wind-jet axis rotating over time. Although average wind-speed values derived from the X-band SAR were in reasonable agreement with model data, maxima values were underestimated. Similarly, inferred wave information was consistent with model results and provided evidence of the spatial evolution of shoaling and refracting waves in the nearshore. This is in support of the idea of Li *et al.* (2009) that high-resolution TerraSAR-X imagery is a particularly good tool to observe the spatial variability of coastal ocean-wave behaviour.

Additional analysis on the spatial evolution of SAR image intensity spectral peaks located 60–120 km away from the coast in the downwind direction suggest the presence of wave energy propagating to the west–southwest, closely aligned with the offshore blowing winds. Comparison of the corresponding wavelengths to parametric wave-prediction relations proposed by Kahma and Calkoen (1992) showed that the secondary peak values derived from the SAR analyses are larger than

predicted. Since a number of relevant explanations for these deviations have risen, further analyses are required, and will be conducted in the near future. A small exercise following Alpers *et al.* (1981) demonstrated that two out of three cases of steep fetch-limited waves generated by the strong gap winds at the Gulf of Tehuantepec lie within the nonlinear regime of the SAR image formation, but close to its limit when the reasonable value of $C = 0.3$ was established. Based on these results, we suggest that a wave-inversion scheme, similar to the ones long proposed for the C-band SAR carried out on European satellites and extensively validated, is desirable to properly derive true wave parameters from TerraSAR-X imagery.

Acknowledgements

This study was developed as part of an academic stay at the Remote Sensing Institute, DLR, under the supervision of Dr S. Lehner. Our profound gratitude to the people in IMF-DLR who contributed to the success of this work: Dr T. König, Y. Ren, P. Held and T. Hantl. Special thanks to Dr P. Osuna from DPO-CICESE and Dr W. Rosenthal from GAUSS mbH for their revisions and comments to the manuscript. We gratefully acknowledge T. Bruns from DWD for providing access to the Global Wind and Wave data. This study was possible thanks to support from the Mexican Government (*Programa de Becas-Mixtas*, CONACYT; DirocIOA project 62520), UABC (*Departamento de Cooperación Internacional e Intercambio Académico*) and DLR (project *Synergy of ocean remote sensing information in oceanic and coastal waters: direct applications from DLR receiving antenna station in Chetumal, QR, Mexico*). Access to TerraSAR-X was possible through project OC-0506 *Study of ocean wave-spectrum evolution under gap-wind and hurricane conditions on Mexican coastal waters using high resolution TerraSAR-X imagery*.

References

Alpers, W., Ross, D. and Rufenach, C., 1981, On the detectability of ocean surface waves by real and synthetic aperture radar. *Journal of Geophysical Research*, **86**, pp. 6481–6498.

Álvarez, L., Badán-Dangón, A. and Valle, A., 1989, On coastal currents off Tehuantepec. *Estuarine, Coastal and Shelf Science*, **29**, pp. 89–96.

Ardhuin, F. and Jenkins, A., 2005, On the effect of wind and turbulence on ocean swell. *Proceedings of The Fifteenth (2005) International Offshore and Polar Engineering Conference*. Seoul, Korea, June 19–24, 2005, pp. 429–434.

Ardhuin, F. and Jenkins, A., 2006, On the interaction of surface waves and upper ocean turbulence. *Journal of Physical Oceanography*, **36**, pp. 551–557.

Ardhuin, F., O'Reilly, W., Herbers, T. and Jessen, P., 2003, Swell transformation across the continental shelf - part I: attenuation and directional broadening. *Journal of Physical Oceanography*, **33**, pp. 1921–1939.

Ardhuin, F., Herbers, T., Van Vledder, G.PH., Watts, K.P., Jensen, R. and Graber, H., 2007, Swell and slanting fetch effects on wind wave growth. *Journal of Physical Oceanography*, **37**, pp. 908–931.

Beal, R., Tilley, D. and Monaldo, F., 1983, Large- and small-scale spatial evolution of digitally processed ocean wave spectra from SEASAT SAR. *Journal of Geophysical Research*, **88**, pp. 1761–1778.

Beal, R., Gerling, T., Irvine, D., Monaldo, F. and Tilley, D., 1986, Spatial variations of ocean wave directional spectra from the SEASAT SAR. *Journal of Geophysical Research*, **91**, pp. 2433–2449.

Brusch, S., Lehner, S., Fritz, T., Soccorsi, M., Solovien, A., and van Schie, B., 2010, Ship surveillance with TerraSAR-X. *IEEE Transactions in Geoscience and Remote Sensing*, in print.

Brusch, S., Lehner, S. and Schulz-Stellenfleth, J., 2008, Synergetic use of radar and optical satellite images to support severe storm prediction for offshore wind farming. *Journal of Selected Topics in Applied Earth Observations and Remote Sensing*, **1**, pp. 57–66.

Center for Satellite Exploitation and Research (CERSAT), 2002, *QuikSCAT Scatterometer Mean Wind Field Products - User Manual*. Version 1.0., Document C2-MUT-W-03-IF. IFREMER, February 2002.

Chelton, D., Freilich, M. and Esbensen, S., 2000, Satellite observations of the wind jets off the Pacific Coast of Central America - part I: case studies and statistical characteristics. *Monthly Weather Review*, **128**, pp. 1993–2018.

Collard, F., Ardhuin, F. and Chapron, B., 2005, Extraction of coastal ocean wave fields from SAR images. *Journal of Oceanic Engineering*, **30**, pp. 526–533.

Collard, F., Mouche, A., Chapron, B., Danillo, C. and Johannessen, J., 2008, Routine high resolution observation of selected major surface currents from space. In *Proceedings of SeaSAR 2008*, 21–25 January 2008, Frascati, Italy (ESA SP-656).

Díaz Méndez, G., Ocampo-Torres, F.J., Osuna, P., García, H. and Durazo, R., 2008, Effects of gap-winds on multi-modal ocean swell systems at the south Pacific Coast of Mexico. In *Proceedings of SeaSAR 2008*, 21–25 January 2008, Frascati, Italy (ESA SP-656).

Donelan, M.A. and Pierson Jr., W.J., 1987, Radar scattering and equilibrium ranges in wind-generated waves with application to scatterometry. *Journal of Geophysical Research*, **92**, pp. 4971–5029.

Engen, G. and Johnsen, H., 1995, SAR ocean wave inversion using image cross spectra. *IEEE Transactions in Geoscience and Remote Sensing*, **33**, pp. 1047–1056.

Fritz, T. and Eineder, M., 2008, *TerraSAR-X Ground Segment Basic Product Specification Document*. Cluster Applied Remote Sensing, DLR. Document TX-GS-DD-3302, issue 1.5.

García-Nava, H., Ocampo-Torres, F.J., Osuna, P. and Donelan, M.A., 2009, Wind stress in the presence of swell under moderate to strong wind conditions. *Journal of Geophysical Research*, **114**, C12008.

Hasager, C.B., Astrup, P., Nielsen, M., Christiansen, M.B., Badger, J., Nielsen, P., Sørensen, P.B., Barthelmie, R.J., Pryor, S.C. and Bergström, H., 2007, *SAT-WIND Project – Final Report*. Risø-R-1586, Risø National Laboratory, Technical University of Denmark.

Hasselmann, K. and Hasselmann, S., 1991, On the non-linear mapping of an ocean wave spectrum into a Synthetic Aperture Radar image spectrum and its inversion. *Journal of Geophysical Research*, **96**, pp. 10 713–10 729.

Hasselmann, S., Heimbach, P. and Bennefeld, C., 1998, *The WASAR Algorithm for Retrieving Ocean Wave Spectra from SAR Image Spectra*. Technical Report 14, Deutsches Klimarechenzentrum.

Hasselmann, S., Brüning, C., Hasselmann, K. and Heimbach, P., 1996, An improved algorithm for the retrieval of ocean wave spectra from synthetic aperture radar image spectra. *Journal of Geophysical Research*, **101**, pp. 16 615–16 629.

Hersbach, H., Stoffelen, A. and De Haan, A., 2005, *CMOD5: an Improved Geophysical Model Function for ERS C-band Scatterometry*. ECMWF Internal Report no. 395.

Horstmann, J., Lehner, S., Koch, W. and Tonboe, R., 2000, Computation of wind vectors over the ocean using spaceborne Synthetic Aperture Radar. *John Hopkins APL Technical Digest*, **21**, pp. 100–107.

Horstmann, J., Koch, W., Thompson, D.R. and Graber, H., 2006, Observation of hurricane winds using Synthetic Aperture Radar. In *Proceedings of SeaSAR 2006*, 23–26 January 2006, Frascati, Italy (ESA SP-613).

Hwang, W., Johannessen, J., Alpers, W., Yang, J. and Gan, J., 2008, Spatial and temporal variations of internal wave sea surface signatures in the northern South China Sea

studied by spaceborne SAR imagery. In *Proceedings of SeaSAR 2008*, 21–25 January 2008, Frascati, Italy (ESA SP-656).

Irvine, D. and Tilley, D., 1988, Ocean wave directional spectra and wave-current interaction in the Agulhas from the shuttle imaging radar-B synthetic aperture radar. *Journal of Geophysical Research*, **93**, pp. 15 389–15 401.

Johannessen, J., Shuchman, R., Lyzenga, D., Wackerman, C., Johannessen, O. and Vachon, P., 1996, Coastal ocean fronts and eddies imaged with ERS-1 synthetic aperture radar. *Journal of Geophysical Research*, **101**, pp. 6651–6667.

Kahma, K. and Calkoen, C., 1992, Reconciling discrepancies in the observed growth of wind-generated waves. *Journal of Physical Oceanography*, **22**, pp. 1389–1405.

Katsaros, K., Vachon, P., Liu, T. and Black, P., 2002, Microwave remote sensing of tropical cyclones from space. *Journal of Oceanography*, **58**, pp. 137–151.

Krogstad, H.E., Samset, O. and Vachon, P.W., 1994, Generalizations of the non-linear ocean–SAR transform and a simplified SAR inversion algorithm. *Atmosphere – Oceans*, **32**, pp. 61–82.

Li, X., Lehner, S. and He, M., 2008, Ocean wave measurements based on satellite synthetic aperture radar (SAR) and numerical wave model (WAM) data - extreme sea state and cross sea analysis. *International Journal of Remote Sensing*, **29**, pp. 6403–6416.

Li, X., Lehner, S. and Rosenthal, W., 2009, Investigation of ocean surface wave refraction using TerraSAR-X data. *Transactions in Geoscience and Remote Sensing*, **48**, pp. 830–840.

Mastenbroek, C. and De Valk, C.F., 2000, A semiparametric algorithm to retrieve ocean wave spectra from synthetic aperture radar. *Journal of Geophysical Research*, **105**, pp. 3497–3516.

Masuko, H., Okamoto, K., Shimada, M. and Niwa, S., 1986, Measurement of microwave backscattering signatures of the ocean surface using X-band and Ka-band airborne scatterometers. *Journal of Geophysical Research*, **91**, pp. 13 065–13 084.

Ocampo-Torres, F., 2001, On the homogeneity of the wave field in coastal regions as determined from ERS-2 and RADARSAT SAR images of the ocean surface. *Scientia Marina*, **65**, pp. 215–228.

Ocampo-Torres, F. and Vachon, P., 2000, Spatial variations of ocean wave spectra in coastal regions from RADARSAT and ERS synthetic aperture radar images. In *Proceedings 6th International Conference on Remote Sensing for Marine and Coastal Environments*, Charleston, SC. EEUU.

Ocampo-Torres, F.J., Díaz Méndez, G., García, H. and Durazo, R., 2007, Ocean-swell spectrum evolution in the Gulf of Tehuantepec, Mexico. In *Proceedings of ENVISAT Symposium 2007*, 23–27 April 2007, Montreux, Switzerland (ESA SP-636).

Ouchi, K., 1994, Modulation of waveheight spectrum and radar cross section by varying surface currents. *IEEE Transactions on Geoscience and Remote Sensing*, **32**, pp. 995–1003.

Reppucci, A., Lehner, S., Schulz-Stellenfleth, J. and Yang, C., 2008, Extreme wind conditions observed by satellite synthetic aperture radar in the North West Pacific. *International Journal of Remote Sensing*, **29**, pp. 6129–6144.

Schulz-Stellenfleth, J. and Lehner, S., 2004, Measurement of 2-D Sea Surface Elevation Fields using complex synthetic aperture radar data. *IEEE Transactions in Geoscience and Remote Sensing*, **46**, pp. 1149–1160.

Schulz-Stellenfleth, J., Lehner, S. and Hoja, D., 2005, A parametric scheme for the retrieval of two-dimensional ocean wave spectra from synthetic aperture radar look cross spectra. *Journal of Geophysical Research*, **110**, p. C05004.

Snodgrass, F.E., Groves, G.W., Hasselmann, K., Miller, G.R., Munk, W.H., and Powers, W.H., 1996, Propagation of ocean swell across the Pacific, *Proceeding of the Royal Society of London*, **A249**, pp. 431–497.

STOFFELEN, A. and ANDERSON, D., 1997, Ambiguity removal and assimilation of scatterometer data, *Quarterly Journal of the Royal Meteorological Society*, **123**, pp. 491–518.

VACHON, P.W. and DOBSON, F.W., 1996, Validation of wind vector retrieval from ERS-1 SAR images over the ocean. *The Global Atmosphere and Ocean System*, **5**, pp. 177–187.

VESECKY, J. and STEWART, R., 1982, The observation of ocean surface phenomena using imagery from the Seasat synthetic aperture radar: an assessment. *Journal of Geophysical Research*, **87**, pp. 3397–3430.

VIOLANTE-CARVALHO, N., OCAMPO-TORRES, F.J. and ROBINSON, I.S., 2004, Buoy observations of the influence of swell on wind waves in the open ocean, *Applied Ocean Research,* **26**, pp. 49–60.

WAMDI GROUP: HASSELMAN, K., HASSELMAN, S., JANSSEN, P.A.E.M., KOMEN, G.J., BERTOTTI, L., LIONELLO, P., GUILLAUME, A., CARDONE, V.C., GREENWOOD, J.A., REISTAD, M., ZAMBRESKY, L. and EWING, J.A., 1988, The WAM model –a third generation ocean wave prediction model. *Journal of Physical Oceanography*, **18**, pp. 1775–1810.